PHYSICAL REVIEW C VOLUME 15, NUMBER 4 APRIL 1977

Time-dependent Hartree-Fock calculations for $^{16}O + {}^{16}O$ and $^{40}Ca + {}^{40}Ca$ reactions*

S. E. Koonin†
Kellogg Radiation Laboratory, California Institute of Technology, Pasadena, California 91125

K. T. R. Davies, V. Maruhn-Rezwani, H. Feldmeier,‡ and S. J. Krieger§
Oak Ridge National Laboratory, Oak Ridge, Tennessee 37830

J. W. Negele¶
Laboratory for Nuclear Science and Department of Physics, Massachusetts Institute of Technology, Cambridge, Massachusetts 02135
(Received 20 September 1976)

The time-dependent Hartree-Fock approximation is applied to $^{16}O + {}^{16}O$ and $^{40}Ca + {}^{40}Ca$ reactions. An effective interaction which results in a local Hartree-Fock potential is used. The full time-dependent Hartree-Fock problem is reduced to two dimensions by treating the relative orbital motion of the ions in the rotating frame approximation. The detailed dynamics of the nuclear density matrix during these reactions is discussed. The deflection function, energy loss, fragment charge distribution, and ion-ion potential have been computed for several reactions and compared with available data. The physical content and limitations of our calculations are discussed.

[NUCLEAR REACTIONS $^{16}O(^{16}O, x)$ and $^{40}Ca(^{40}Ca, x)$ in time-dependent Hartree-Fock approximation. Fusion and strongly damped collisions.]

I. INTRODUCTION

During recent years, there has been renewed interest in the derivation and application of microscopic theories of collective motion for quantal many-body systems. This interest has been particularly strong in nuclear physics, for which heavy-ion reactions are providing a rapidly increasing body of high quality experimental data. The ultimate goal of any microscopic theory of nuclear motion is to provide a unified description of the reaction dynamics over a wide range of physical phenomena, including large amplitude oscillations, fission, fusion, and compound nucleus formation. Some of the methods used to describe these processes include resonating groups,[1] generator coordinates,[2] the random phase approximation (RPA),[3] adiabatic time-dependent Hartree-Fock (ATDHF),[4] and fluid dynamics.[5] None of these, however, is without its drawbacks. For example, computational complexities prohibit the application of the resonating group method to all but the lightest nuclei. With generator coordinates, it has been found necessary to impose on the system, *a priori*, selected collective degrees of freedom in order to make calculations feasible. The RPA is a linearized approximation to time-dependent Hartree-Fock (TDHF), and is thus applicable only to small amplitude disturbances. The ATDHF is certainly limited to the description of low-lying excitations in the case of large amplitude motion,[6] and there may even be further restrictions on the amplitude of excitations.[7] Finally, the application of fluid dynamics to nuclei depends upon approximations whose validity can be tested only by a more complete microscopic theory.[8]

One method for treating nuclear dynamics that merits serious consideration is a direct solution of the TDHF equations, which were first proposed by Dirac nearly 50 years ago.[9] This approximation consists of assuming that the many-body wave function can be described by a single Slater determinant. There are many motivations for applying this approximation to nuclei.[10] First, TDHF is a microscopic theory, requiring as input only an effective internucleon interaction and initial conditions; it is unnecessary to make any assumptions about the relevant collective or intrinsic coordinates. Moreover, because TDHF is a quantal independent-particle approximation, it admits to a semiclassical interpretation, thus offering insight not obtainable in calculations using more complicated wave functions. The possibility that TDHF provides meaningful results is enhanced by the significant successes that static Hartree-Fock (HF) theory has enjoyed in providing descriptions of the binding energies and charge densities of ground states.[11] Furthermore, the RPA using the same effective interactions has provided an adequate description of the properties of low-lying excited states.[12] Finally, we note that an investigation of the TDHF approach will necessarily lead to a better understanding of methods based upon TDHF, such as RPA and ATDHF, and the relation

between it and fluid dynamics.

The initial application of the TDHF approximation to reactions between semi-infinite slabs of nuclear matter[10] produced a rich collision phenomenology which included compound "nucleus" formation, resonances, and highly inelastic reactions. The dynamics were conspicuously dominated by the propagation and reflection of single-particle wave functions in the mean HF potential. At low energies this single-particle behavior resulted in a delicate transition between the scission and fusion of oscillating compound slabs. At higher energies the single-particle orbitals were predominantly transmitted with distortion through the compound system, resulting in the dissipation of roughly 90% of the initial translational kinetic energy and significant modulation of the originally smooth density. Although it was hoped that much of the underlying physics had emerged in the one-dimensional geometry, the question remained as to what extent the single-particle dynamics and collision phenomenology would persist in a more realistic calculation. This question, and the ability to provide a microscopic realization of heavy-ion reaction phenomena, has encouraged the further application of TDHF[13, 14] and motivates the present work.

This paper presents a systematic study of $^{16}O+^{16}O$ and $^{40}Ca+^{40}Ca$ reactions in the TDHF approximation.[15] These systems are treated under the additional approximations that the colliding nuclei retain an axis of symmetry about the line joining their mass centers and that the relative orbital angular momentum is conserved. While these approximations are rigorously true only for zero-impact parameter collisions, they are also sensible for grazing collisions and are related to a more general variational theory.

The paper is organized as follows. Section II describes the effective interaction used in the calculations and the axial symmetry approximation. Calculational details are discussed in Appendixes A–C. Section III presents the results and makes comparisons with available experimental data. Finally, Sec. IV contains a brief summary and conclusions.

II. TDHF EQUATIONS

A. Effective interaction

The effective interaction used in our calculations consists of the modified Skyrme force used in Ref. 10, plus the Coulomb interaction. The total energy for a spin-saturated, charge-symmetric nucleus may be written as

$$H = H_n + H_C \,, \tag{2.1}$$

where H_n is the nuclear energy and H_C the Coulomb energy. The nuclear energy has the form

$$H_n = \int d^3r \left[\frac{\hbar^2}{2m} \tau(\vec{\mathbf{r}}) + \tfrac{3}{8} t_0 \rho^2(\vec{\mathbf{r}}) + \frac{t_3}{16} \rho^3(\vec{\mathbf{r}}) \right] + \tfrac{1}{2} V_0 \int d^3r \int d^3r' \rho(\vec{\mathbf{r}}) \frac{e^{-|\vec{\mathbf{r}}-\vec{\mathbf{r}}'|/a}}{|\vec{\mathbf{r}}-\vec{\mathbf{r}}'|/a} \rho(\vec{\mathbf{r}}'). \tag{2.2}$$

The two densities appearing in this expression are the particle density

$$\rho(\vec{\mathbf{r}}) = \sum_{i=1}^{A} |\psi_i(\vec{\mathbf{r}})|^2 \,, \tag{2.3}$$

and the kinetic energy density

$$\tau(\vec{\mathbf{r}}) = \sum_{i=1}^{A} |\nabla \psi_i(\vec{\mathbf{r}})|^2 \,, \tag{2.4}$$

where the $\psi_i(\vec{\mathbf{r}})$ are the complex single-particle wave functions of the Slater determinant. The parameters t_0, t_3, V_0, and a are taken from Table I of Ref. 10.

For the Coulomb energy, we take

$$H_C = \frac{e^2}{8} \int d^3r \int d^3r' \rho(\vec{\mathbf{r}}) \frac{1}{|\vec{\mathbf{r}}-\vec{\mathbf{r}}'|} \rho(\vec{\mathbf{r}}'). \tag{2.5}$$

Note that in addition to assuming equal proton and neutron densities, we have neglected the Coulomb exchange energy.

The variation of the energy functional (2.1) with respect to the single-particle wave functions straightforwardly yields the TDHF equations[16]

$$i\hbar \frac{\partial \psi_j}{\partial t} = h\psi_j \,, \quad j = 1, 2, \ldots, A. \tag{2.6}$$

The HF Hamiltonian h is

$$h = -\frac{\hbar^2}{2m} \nabla^2 + W(\vec{\mathbf{r}}), \tag{2.7}$$

and the HF potential W is

$$W(\vec{\mathbf{r}}) = \tfrac{3}{4} t_0 \rho(\vec{\mathbf{r}}) + \tfrac{3}{16} t_3 \rho^2(\vec{\mathbf{r}}) + V_0 \int d^3r' \frac{e^{-|\vec{\mathbf{r}}-\vec{\mathbf{r}}'|/a}}{|\vec{\mathbf{r}}-\vec{\mathbf{r}}'|/a} \rho(\vec{\mathbf{r}}') + \frac{e^2}{4} \int d^3r' \frac{1}{|\vec{\mathbf{r}}-\vec{\mathbf{r}}'|} \rho(\vec{\mathbf{r}}'). \tag{2.8}$$

The effective interaction used, which does include exchange effects in the nuclear force, has been shown to provide a reasonable reproduction of binding energies, radii, and densities for ^{16}O and ^{40}Ca.[10] The other Skyrme forces, which result in nonlocal HF potentials, give better fits to the experimental charge densities. Although the densities obtained with our local HF potential may be somewhat improved by a suitable readjustment of the parameters, we believe this would be unwarranted at present since the effect of nonlocality on nuclear dynamics remains an open question. We are presently investigating reactions with non-

local Skyrme forces and will report the results in a future publication.

B. Axial symmetry approximation

If the TDHF equations are to be solved in full, then it is only necessary to integrate Eqs. (2.6) with a given set of initial conditions in order to determine the TDHF wave function. This is not impossible for the systems we treat here.[14, 17] However, because of the large amounts of computer time required for even these simple three-dimensional calculations, we have reduced the TDHF problem to two nontrivial dimensions by enforcing the restriction that the colliding nuclei retain axial symmetry about the rotating line joining their mass centers. For mass-symmetric systems, we work in the intrinsic, body fixed frame and add to the energy functional (2.1) the classical energy of rotation:

$$H' = H + \frac{L^2}{2I[\rho]} . \tag{2.9}$$

Here, $L = (l + \frac{1}{2})\hbar$ is the conserved relative orbital angular momentum along the rotation axis perpendicular to the scattering plane and the moment of inertia $I[\rho]$ is a prescribed functional of the density. The presence of this term in the energy functional results in a corresponding addition to the HF potential (2.8):

$$W'(\vec{r}) = W(\vec{r}) - \tfrac{1}{2}\omega^2 \frac{\delta I}{\delta \rho(\vec{r})} , \tag{2.10}$$

$$\omega = \frac{d\theta}{dt} = \frac{L}{I[\rho]} , \tag{2.11}$$

where we have defined the rate of rotation of the symmetry axis ω. Note that the as yet unassessed effects of Coriolis forces are neglected in this approximation, and only centrifugal forces are included.

When the colliding nuclei are far apart, as defined by the criterion that the density at the center of mass (taken to be the origin) is less than the clutching density ρ_c, the moment of inertia is calculated as that of two point masses:

$$I[\rho] = \tfrac{1}{4} m A R^2, \quad \rho < \rho_c , \tag{2.12}$$

where the separation coordinate R is

$$R = \frac{2}{A} \int d^3r \, |z| \, \rho(\vec{r}), \tag{2.13}$$

and A the total mass number of the two ions. When the density at the origin exceeds ρ_c, the nuclei are assumed to have clutched, and the moment of inertia is taken to be that of a rigid body:

$$I[\rho] = m \int d^3r \, \rho(\vec{r})(z^2 + r_\perp^2 \cos^2\phi)$$

$$= 2\pi m \int dz \, r_\perp \, dr_\perp \, \rho(r_\perp, z)(z^2 + \tfrac{1}{2} r_\perp^2). \tag{2.14}$$

We have taken $(r_\perp, z, \phi)$ as the cylindrical coordinates. Variation of the moment of inertia with respect to the density then leads to the result

$$W'(r_\perp, z) = \begin{cases} W(r_\perp, z) - \tfrac{1}{2} m\omega^2 R\,|z|, & \rho(0,0) < \rho_c , \\ W(r_\perp, z) - \tfrac{1}{2} m\omega^2 (z^2 + \tfrac{1}{2} r_\perp^2), & \rho(0,0) > \rho_c . \end{cases} \tag{2.15}$$

Calculations have proven insensitive to the exact value of ρ_c. We have taken $\rho_c = 0.07$ fm^{-3}, approximately one-half of the saturation density of nuclear matter with our effective interaction. With the replacement of W by W', Eqs. (2.6) are solved to determine the TDHF wave function, and Eq. (2.11) specifying the time variation of ω simultaneously integrated to obtain the orientation of the symmetry axis in space.

The axial approximation we have described above is clearly valid for exactly head-on collisions and for noninteracting trajectories. One would also expect it to be valid for grazing trajectories, in which large portions of the system do not suffer interaction, and for near head-on collisions which retain approximate axial symmetry. Of course, the validity of these approximations can ultimately be tested only by comparison with fully three-dimensional calculations.[17]

It is worthwhile to note that the axial approximation we have adopted has two distinct aspects. The first is the definition of $I[\rho]$, which involves both the assumption of rigid body rotation and a prescription for clutching. As an alternative to this treatment of the orbital motion, the problem may be formulated in a wider variational sense, allowing for the most general determinant with an axially symmetric density and a common, nonaxial, velocity potential for all of the single-particle wave functions.[18] Thus, the approximation for the moment of inertia we have used is not essential, and the more general variational calculations are presently being carried out.

The second aspect of our approximation is the constraint to an axially symmetric density. This is crucial to the reduction of the problem to two nontrivial dimensions, and has both macroscopic and microscopic implications. Macroscopically, the collision of two liquid drops may lead to a nonaxial compound system. Here, the restriction to axial symmetry is probably not too serious, since the energy difference between the true shape and the nearest axial shape should not be too large. However, the liquid drop may scission in

a nonaxial manner, rather than as toroidal fragments which are rotationally invariant about a specified axis. The fragments in the final state may then tumble with different amounts of intrinsic angular momentum in each. Thus axial symmetry limits the range of accessible final states and loses any information concerning the distribution of final angular momenta.

Microscopically, additional reservations concerning our axially symmetric calculations may arise in connection with fusion. In TDHF, fusion occurs if collisions of the single-particle wave functions with the walls of the HF potential can randomize and equilibrate the initially coherent orbitals sufficiently to prevent fragment escape. This equilibration would be expected to occur more rapidly in a potential well possessing no special symmetries than in our axially symmetric HF potentials. Thus, one may expect that the freezing of transverse degrees of freedom would result in an underestimation of dissipation and equilibration in those collisions for which nonaxial degrees of freedom are important.[17]

Since we treat mass-symmetric systems, the initial TDHF wave function is reflection symmetric through the plane $z=0$ containing the center of mass. Because this symmetry and the axial symmetry we impose are also symmetries of the energy functional (2.1), they are conserved by the TDHF solution. Thus, z parity and m, the angular momentum projection on the z axis, are good quantum numbers for the spatial single-particle wave functions. In addition, the $(r_\perp, z)$ dependence of wave functions having $\pm m$ in the same orbital is identical. When the additional spin and isospin symmetries are included, only six spatial wave functions must be evolved for $^{16}O+^{16}O$: the positive and negative z-parity combinations of the $1s$, $1p_{m=0}$, and $1p_{m=\pm1}$ orbitals for a single ^{16}O nucleus. For ^{40}Ca reactions, one additionally needs the positive and negative z-parity combinations of the $2s$, $1d_{m=0}$, $1d_{m=\pm1}$, and $1d_{m=\pm2}$ orbitals. The definite z parity of all orbitals limits numerical work to the half-space $z \geq 0$.

Initial conditions for the TDHF wave functions were taken to be the HF ground states of the reacting ions,[19] separated by a distance far greater than the sum of the nuclear radii and boosted by a uniform velocity field corresponding to the initial relative velocity. Initial values for θ (the frame orientation), the initial relative velocity, and the final values of the scattering angle and fragment kinetic energies were obtained by matching to point Coulomb trajectories before and after the calculated collision. The numerical methods used to integrate the TDHF equations are discussed in detail in Appendixes A and B.

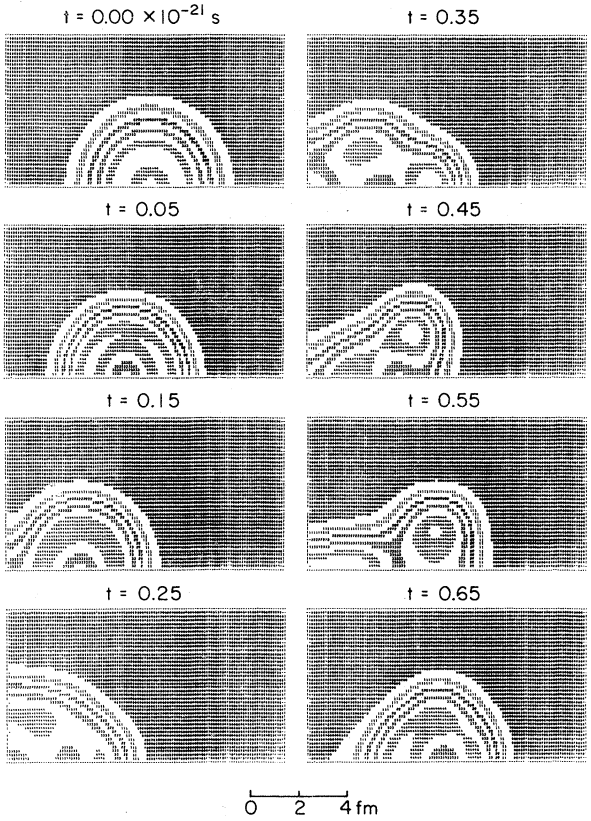

FIG. 1. Density contour maps for a head-on $^{16}O+^{16}O$ collision at a center-of-mass bombarding energy of $E/A=2$ MeV (lab energy = 8 MeV/projectile nucleon). The collision is shown in the center-of-mass frame. Because of the rotational symmetry about the horizontal (z) axis and reflection symmetry through the vertical plane ($z=0$ plane), only the density for $z \geq 0$ is shown. The contour stripes mark density intervals of 0.04 nucleons per fm^3. For times later than $t=0.65\times10^{-21}$ s, the fragments separate while oscillating in a predominantly octupole mode. This figure was actually calculated with no Coulomb or Yukawa forces and harmonic oscillator initial conditions, using the modified two- and three-body strengths $t_0=-1090.0$ MeV fm^3 and $t_3=17288.0$ MeV fm^6, respectively. A collision calculated with Hartree-Fock initial conditions and the full force of (2.8) yields results qualitatively indistinguishable from these, except for the slight monopole oscillations prior to collision.

III. RESULTS

A. Time-dependent densities

Figure 1 presents contour plots of the time-dependent nucleon density $\rho(\vec{r}, t)$, for a head-on $^{16}O+^{16}O$ reaction at a center-of-mass bombarding energy per nucleon $E/A=2$ MeV.[13] Here E refers to the total translational energy in the center-of-mass frame. The bombarding energy in the lab-

oratory frame is twice as great: In this case $E_{lab} = 2 \times 32 \times 2$ MeV = 128 MeV. The ions interpenetrate at $t \sim 0.2 \times 10^{-21}$ s. Separation then begins, apparently initiated by a surface bulge which travels outward from the $z = 0$ plane ($t \sim 0.3 - 0.5 \times 10^{-21}$ s). Finally, a neck forms, and scission occurs ($t \sim 0.6 - 0.7 \times 10^{-21}$ s), with the fragments moving apart with greatly reduced translational kinetic energy. Of particular note are the toroidal configurations of the nascent fragments ($t \sim 0.5 \times 10^{-21}$ s), the large octupole amplitude in the post scission vibrations, and the constancy of the surface diffuseness throughout the reaction. It should also be remarked that several features of the dynamics indicate deviations from the commonly assumed irrotational velocity pattern,[5] as discussed subsequently.

Because of the importance of single-particle dynamics in the slab collisions of Ref. 10, it is important to investigate single-particle effects in the present, more realistic geometry. Before proceeding, however, it must be emphasized that any discussion of single-particle orbitals is highly representation dependent, since the TDHF equations (and all observables) may be expressed in terms of the representation-independent, one-body density matrix. In the present geometry, the wave functions may be arbitrarily scrambled by any unitary transformation. For example, since ^{16}O and ^{40}Ca are spherically symmetric before the collisions, the angular dependence of the single-particle wave functions may be referred to an arbitrarily oriented axis, so that phenomena previously associated with the $1p_{m=0}$ orbital would become a complicated superposition of effects due to the $1p_{m=0}$ and $1p_{m=\pm1}$ orbitals. Other transformations would, of course, obscure the physics even more. Faced with the nonuniqueness of the single-particle wave functions, our rationale has been to pick a representation in which the dynamics are as simple and obvious as possible. The optimal basis is one which exploits the axial and reflection symmetries of the system and naturally emphasizes the coherencies of the initial determinant. In fact, this basis is the one in which the calculation is actually performed. In contrast to the case of slab geometry,[10] it is not practical to graph each of the single-particle wave functions involved, and so the following discussion is qualitative in nature.

In the basis chosen, the initial HF description of a single ^{16}O nucleus requires four orbitals: a $1s$ orbital, whose density is approximately Gaussian about the center of the nucleus; a $1p_{m=0}$ orbital, whose density appears as two lobes on the z axis on either side of the $1s$ orbital; and the $1p_{m=\pm1}$ orbitals, each of which has a density which is a torus about the z axis encircling the $1s$ Gaussian. Before contact, the orbitals for each nucleus are confined by their respective self-consistent potentials. However, upon contact, the barrier between the nuclei in the full HF potential disappears. The wave functions from each nucleus then move across the $z = 0$ plane toward the other side. As the $1p_{m=0}$ orbital has the highest momentum components in the z direction, it is expected to lead the other orbitals across the compound system. This is indeed the case, as may be seen at time $t = 0.35 \times 10^{-21}$ s, where the $1p_{m=0}$ orbital from the left hand nucleus is hitting the right wall of the system, while the $1p_{m=\pm1}$ torus from the left side trails behind. At $t = 0.45 \times 10^{-21}$ s, the $m = 0$ orbital has bounced and moves leftward through the torus, which continues moving toward the right wall. The motion of the $1p_{m=0}$ orbital causes a reflooding of the neck at $t = 0.55 \times 10^{-21}$ s. Finally, at scission the $1p_{m=\pm1}$ orbitals are on the opposite sides from which they originated, while the $1p_{m=0}$ orbitals have returned to their original sides. Although the $1s$ orbitals are not apparent in the plot, they are expected to move with the $1p_{m=\pm1}$ torus. Even though the single-particle wave functions themselves have no physical meaning, owing to the antisymmetry of the nuclear wave function, their dynamics strongly governs the density observed in the collision process.

From the above discussion, it is evident that there are deviations from irrotational flow. At $t = 0.45$ the upper $1p_{m=\pm1}$ torus is moving to the right while the lower $1p_{m=0}$ orbital is moving to the left. In the region between the torus and the $1p_{m=0}$ orbital, $\partial v_z / \partial r \neq 0$ and since $\partial v_r / \partial_z \approx 0$, it is clear that $\nabla \times \vec{v} \neq 0$.

Figure 2 displays contour plots of the density for a head-on ^{40}Ca + ^{40}Ca reaction at a center-of-mass bombarding energy of 2 MeV per nucleon ($E_{lab} = 320$ MeV). At $t = 0$, the nuclei are well separated and interact only through the Coulomb potential. At $t = 0.16 \times 10^{-21}$ s, the densities of the two nuclei have just begun to overlap strongly. Their speeds at this point have not been greatly diminished. By $t = 0.32 \times 10^{-21}$ s, the nuclei have completely coalesced. The centers of the two mass distributions are now moving apart with a speed approximately equal to $\frac{1}{3}$ the initial speed of approach. In the time interval from $t = 0.48 \times 10^{-21}$ s to $t = 0.80 \times 10^{-21}$ s, the nuclear mass is greatly elongated, a neck has formed, and shape oscillations are apparent. At $t = 0.96 \times 10^{-21}$ s, the necking has become quite pronounced, and by $t = 1.12 \times 10^{-21}$ s, the nuclei have separated, and move apart with a relative speed equal to approximately $\frac{1}{4}$ of the initial speed of approach.

As can be seen, single-particle effects are not

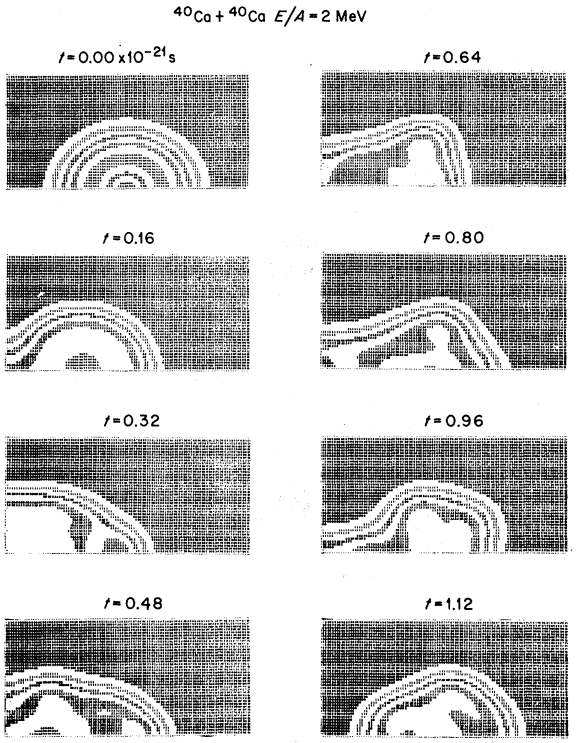

FIG. 2. Similar to Fig. 1 for a head-on $^{40}Ca + ^{40}Ca$ collision at a laboratory bombarding energy of 8 MeV/nucleon. This figure and all those subsequent have been calculated using (2.8).

as strong in $^{40}Ca + ^{40}Ca$ as they are in $^{16}O + ^{16}O$. This is so because the greater number of occupied orbitals in the ^{40}Ca reactions clearly minimize the importance of any single orbital. This result lends credence to the idea that for very large systems, the dramatic clustering effects and density-ripples seen in these and three-dimensional calculations[14] will be minimized.

In Fig. 3, we plot density profiles for the head-on $^{40}Ca + ^{40}Ca$ reaction at a center of mass bombarding energy $E/A = 1$ MeV ($E_{lab} = 160$ MeV). In this case, the nuclei fuse, with the separation coordinates R [defined by (2.13)] undergoing four damped oscillations in the 4×10^{-21} s portrayed. The oscillations are approximately harmonic with a period of 0.8×10^{-21} s. Similar results are obtained for $^{16}O + ^{16}O$ at $E/A = 0.5$ MeV ($E_{lab} = 32$ MeV). In this case, R undergoes six damped oscillations in 4×10^{-21} s, with the period decreasing from 0.6×10^{-21} to 0.4×10^{-21} s. In both cases, we feel we have observed what operationally may be defined as fusion in a TDHF calculation.

Some additional features of the density distribution at finite angular momentum are displayed in Fig. 4, where we have plotted the density in the region $z \geq 0$ for the reaction $^{16}O + ^{16}O$ at a center-of-mass bombarding energy of 3 MeV per particle (12 MeV/nucleon lab) for several values of the relative angular momentum. In each case the solid line denotes the density at the time of closest approach as a function of z for fixed $r_\perp \simeq 0$, while the dashed line represents the uniformly displaced initial density of one of the ^{16}O nuclei. The dashed line has been reflected through $z = 0$, to assist the eye in distinguishing the difference between the calculated density and the sum of the densities of the two noninteracting ^{16}O nuclei.

In the TDHF approximation, the Pauli principle is mediated by the HF potential, in the sense that the reason the originally orthogonal wave functions remain orthogonal is the fact that they are all propagating in the same mean field. Whereas in a semiclassical description, the Pauli principle and potential interactions appear to produce distinct physical effects which can be considered separately, they are necessarily unified in the present theory. As is clear from Figs. 7, 9, and 17 in Ref. 10, simultaneous evolution of orthogonal single-particle wave functions in a common mean field in low energy collisions yields negligible increase in central density consistent with the semiclassical Pauli principle description. This same phenomenon dominates the small impact parameter collisions ($l = 0$ to $l = 25$). At larger impact parameters, $l = 42$, $l = 45$, the central density plays a secondary role and the surface density is significantly increased relative to the noninteracting density by the attractive nuclear potential in the overlap region. The dramatic effects of the mean field that we have observed here will disappear as the ratio of the ion bombarding energy to the depth of the mean field is increased.[13]

In order to make contact with the results of macroscopic calculations,[20] Fig. 5 shows several reaction trajectories in the R-σ plane. The fragment elongation coordinate σ, is defined as[20]

$$\sigma = (\langle z^2 \rangle - \tfrac{1}{4}R^2)^{1/2} ,$$

where $\langle z^2 \rangle$ is taken over the whole system. Note that this differs from the definition of Ref. 20 by a factor of 2. In no case does the system ever reach the liquid drop model single sphere configuration, although at the higher energies and lower angular momenta, there is greater penetration through the single spheroid line and toward the single sphere configuration. After penetration, there is a greater tendency toward prolate shapes for the higher energies at the lower angular momenta, so that scission occurs with more elongated fragments. In macroscopic terms, the

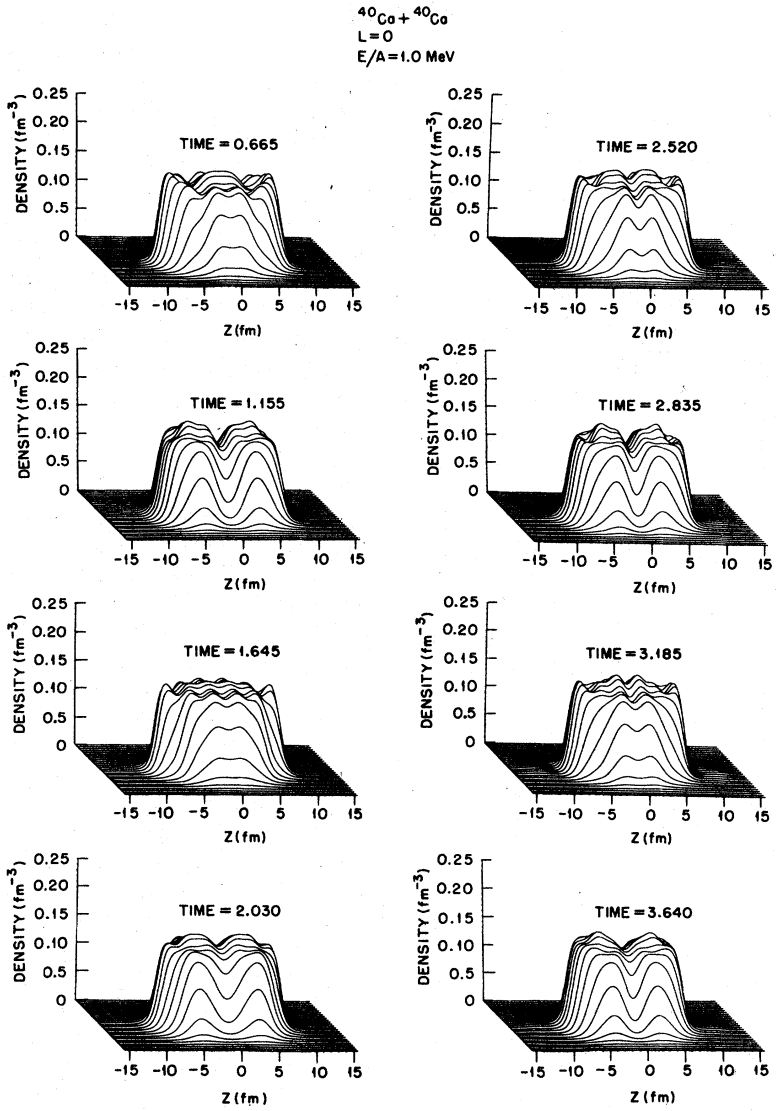

FIG. 3. Density profiles for a head-on $^{40}Ca + ^{40}Ca$ reaction at a laboratory bombarding energy of 4 MeV/nucleon. The density is plotted vertically above the $(r_\perp, z)$ plane. The times, labeled in units of 10^{-21} s, have been chosen to correspond approximately to the maxima and minima of the oscillations of the fused system.

two ^{40}Ca nuclei enter along the fusion valley, and emerge at a higher σ value along the fission valley. The lower energy and higher angular momentum trajectories show a richer structure with a more complex interplay between separation and deformation modes.

The R-σ plot of Fig. 5 succinctly displays a significant physical distinction between the liquid drop and TDHF approaches to nuclear dynamics. The liquid drop theory implicitly assumes an instantaneous isotropic local equilibration of the colliding nucleons, so that the density tends toward a spherical shape after fusion. In TDHF, however, equilibration takes place only via collisions with the walls of the HF potential well, so that longitudinal motion through the system is only slowly equilibrated into the transverse directions. As a result, there is no pressure to deform the well transversely, and the compound TDHF systems remain prolate, as in Figs. 3 and 5. This feature is not an artifact of axial symmetry, since finite impact parameter calculations in three dimensions show a similar tendency toward prolate shapes.[17] Thus, this distinction represents a significant difference between the TDHF and liquid drop approaches, so that it remains a challenge to determine experimental observables which can distinguish this difference.

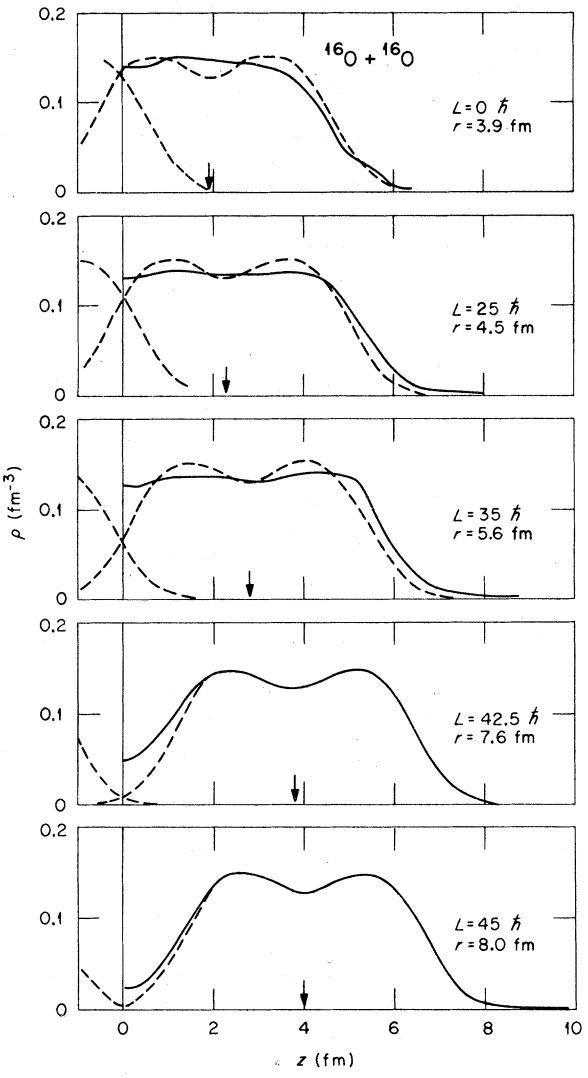

FIG. 4. Density profiles at the time of closest approach for $^{16}O + ^{16}O$ at a laboratory bombarding energy of 12 MeV/nucleon.

B. Experimental observables

While the mean field approximation serves as an adequate starting point for the systematic evaluation of the expectation values of few-body operators, it need not provide sensible information about the full many-body wave function or expectation values of many-body operators. Indeed, it would be absurd to expect information concerning multinucleon correlations from a theory that is fundamentally one body in nature. Fortunately, the few-body properties of isolated nuclei such as the density, binding energy, or spectroscopic factors are well reproduced by the mean-field wave function. However, the computation of reaction cross sections requires S matrix elements, which are the overlap of the full many-body wave function with the relevant channel states. Consequently, one should not expect TDHF to provide cross sections to specific final channels, but rather to yield information concerning the average or most probable properties of reaction processes. It is therefore important to formulate the comparison between TDHF and experiment in terms of expectation values of few-body operators in the TDHF wave function, such as the moments R and σ, the mean fragment translational kinetic energy or angular momentum, or the nucleon number and charge operators. With this caveat, we proceed to compare our calculations with experiment.

In Fig. 6 the R-θ trajectories for $^{16}O + ^{16}O$ collisions at a center of mass bombarding energy of 3 MeV per nucleon (E_{lab} = 192 MeV) and the trajectories for $^{40}Ca + ^{40}Ca$ collisions at a center-of-mass bombarding energy of 1.738 MeV per nucleon (E_{lab} = 278 MeV) are displayed. Each of the trajectories is labeled by l, the relative orbital angular momentum of the trajectory θ_F, the final center-of-mass scattering angle, and E_F, the asymptotic value of the total translational kinetic energy in the center-of-mass system. Qualitatively, the $^{16}O + ^{16}O$ and $^{40}Ca + ^{40}Ca$ trajectories are quite similar. Both systems exhibit what appears to be backscattering for low angular momenta. This is an artifact of the definition of the coordinate R, which can never go through zero. Indeed, it is not unreasonable to expect that the majority of the single-particle wave functions are transmitted through the compound system in these head-on collisions. For larger values of the angular momentum, the trajectories take on a skimming characteristic and then begin to orbit. As the angular momentum is further increased beyond the orbiting value, the attraction of the nuclear potential is almost counterbalanced by the centrifugal and Coulomb repulsion. For l above grazing (~45 for ^{16}O, ~100 for ^{40}Ca), the trajectories are nearly pure Coulomb.

In Fig. 7, the energy loss and scattering angle are plotted as a function of the angular momentum. Note that the plateau of severe energy loss cannot easily be associated with a characteristic type of trajectory. The angular momentum at which orbiting occurs stands out quite dramatically in the deflection function.

In the event that TDHF were to account for the full dissipation observed experimentally, it should be possible to directly compute the fusion cross section from the energy-L plot of Fig. 7. For low l up to the maximum fusion angular momentum l_{fus}, the energy loss should be either undefined (the system sticks together) or equal to the differ-

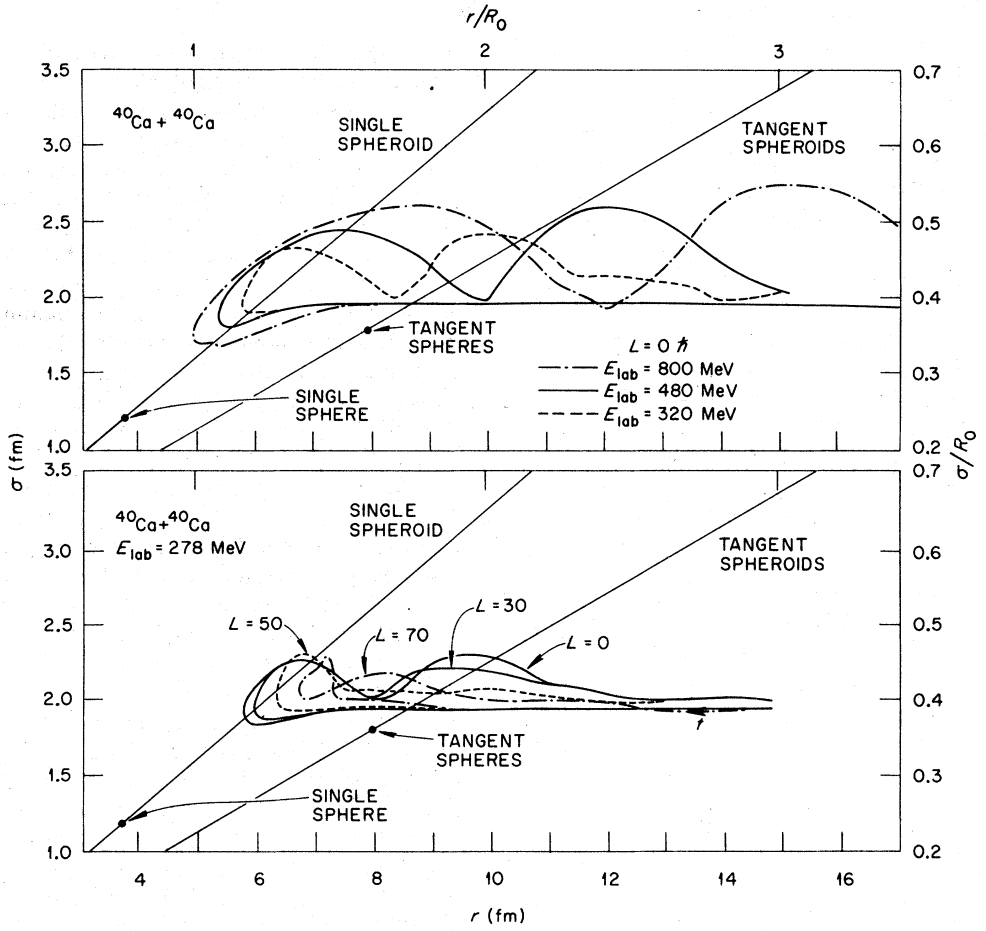

FIG. 5. R-σ trajectories for various $^{40}Ca+^{40}Ca$ reactions. Several features of the liquid drop topography computed with $R_0=1.18\ (80)^{1/3}$ fm are shown, including the lines of spheroids and tangent spheroids.

ence between the initial energy and the Coulomb repulsion energy of the stretched scission configuration in the event that the fragments scission with no relative velocity. Above l_{fus}, but below the very peripheral l for which the energy loss is zero, a direct comparison of the TDHF results with the experimental deep-inelastic events should be possible. Unfortunately, the present calculations show too little dissipation in the region $l=30$ to $l=90$ of the $^{40}Ca+^{40}Ca$ system. For example, no fusion is observed in this region. In addition, with the assumption of two-body kinematics, the total fragment center-of-mass kinetic energy extracted by Colombani *et al.*[21] is approximately 60 MeV at l in the range 70–90, showing roughly twice the energy loss we calculate with TDHF.

C. Charge distributions

As we have discussed, the TDHF wave function is a Slater determinant at all times. Initially, the determinant may be written as the antisymmetrized product of two nonoverlapping determinants describing the separated ions. Thus, at $t=0$ the wave function is an eigenfunction of the operators $\hat{N}_R$ and $\hat{N}_L$ which count the number of nucleons in the region $z\geq 0$ and $z<0$, respectively. Of course, $\hat{N}_R+\hat{N}_L=\hat{N}$, the total number operator. After the reaction, the wave function is no longer an eigenfunction of the separate operators $\hat{N}_R$ and $\hat{N}_L$, but rather only of their sum $\hat{N}$. That is, at any later time t, the wave function will in general be a wave packet containing states with a diverse number of particles in the half space $z\geq 0$ ($z<0$). Asymp-

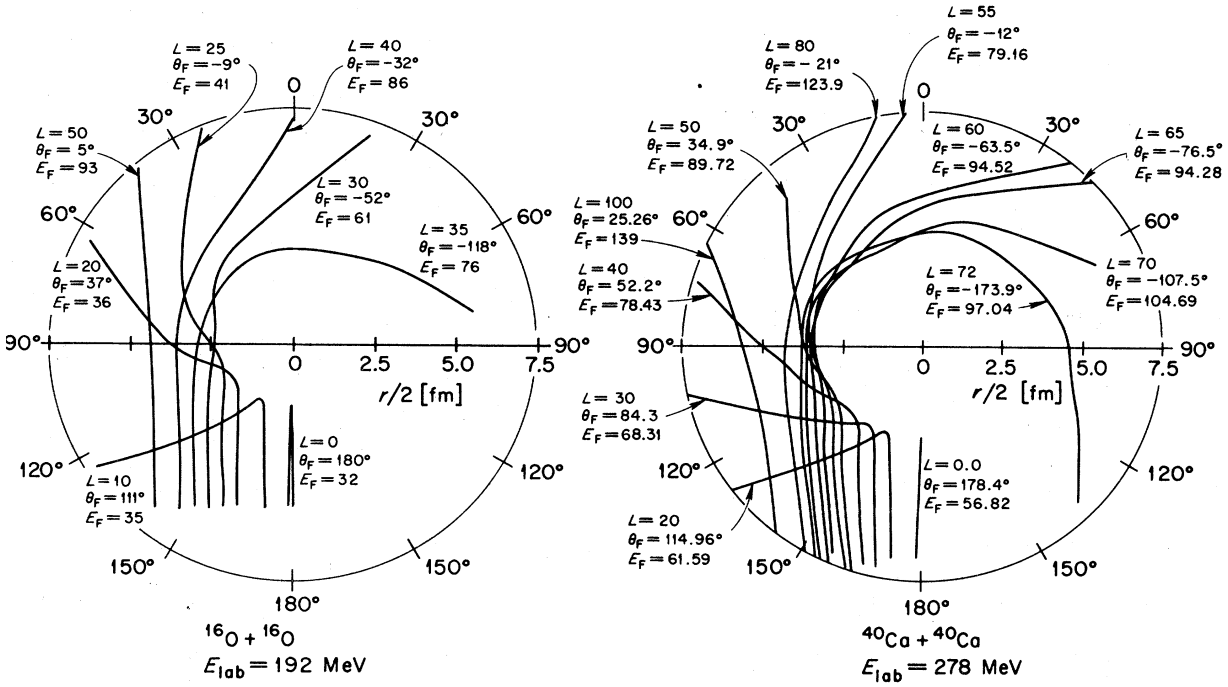

FIG. 6. K-θ trajectories for representative $^{16}O+^{16}O$ and $^{40}Ca+^{40}Ca$ reactions.

totically, the distribution in particle number will be time independent, and we may therefore calculate the probability $[P(A_R)]$ that the final state contains A_R particles in the right half space, and $A_L = A - A_R$ particles in the left hand space. Formally, we may write

$$P(A_R) = \frac{A!}{A_R! A_L!} \int_{-\infty}^{0} dz_1 \cdots dz_{A_L} \times \int_0^{\infty} dz_{A_{L+1}} \cdots dz_A |\Psi|^2, \qquad (3.1)$$

where coordinates other than z are assumed to be integrated out.

As described in Appendix C, we have analyzed the final TDHF wave functions using (3.1) for $^{40}Ca+^{40}Ca$ at a bombarding energy of 278 MeV in the laboratory for several values of the angular momentum. The results of the calculation are presented in Table I, which gives the standard deviation Γ of the charge distribution following the collision. The width is a maximum for head-on collisions, decreases to a minimum as the impact parameter is increased, and then undergoes a slight increase as the impact parameter is further increased to a value corresponding to the

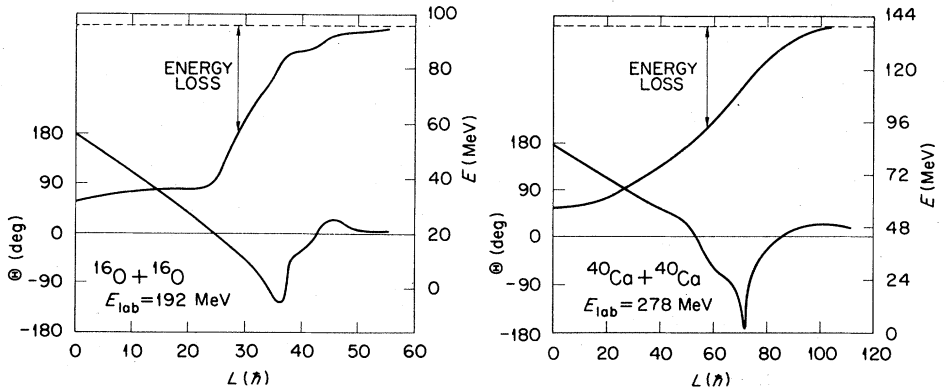

FIG. 7. The deflection and energy-loss functions for the reactions of Fig. 6. The dotted line represents elastic scattering.

TABLE I. Standard deviation of the charge distribution, Γ, for reaction products of ^{40}Ca + ^{40}Ca at E_{lab} = 278 MeV in various partial waves.

l	Γ (charge units)	l	Γ (charge units)
0	2.02	72	1.616
20	1.92	73	1.180
25	1.878	74	1.127
30	1.81	77	0.602
40	1.655	78	0.55
50	1.41	95	0.243
60	1.43	100	0.117
70	1.48	120	0.111

orbiting value of the angular momentum. Further increase in the impact parameter results in an abrupt drop in the width, which goes to zero for the noninteracting trajectories.

To compare these results with the charge distributions measured in Ref. 21, it is necessary to account for the effects of evaporation in the fragments. In Fig. 8 we have reproduced the charge distribution of Ref. 21 measured at $\theta_{c.m.} = 30°$, for which the assumption of two-body kinematics appears justified. Evaporation calculations[22] for excitation energies of the ^{40}Ca nucleus of 31 and 42 MeV, which should bracket the excitation energies in strongly damped events, evidently account for only a small fraction of the observed charge dispersion. Thus, combining the TDHF charge distribution calculated above with subsequent fragment evaporation would yield a total dispersion significantly smaller than that observed experimentally. It is possible that the TDHF width will be increased in calculations which treat neutrons and protons separately.

Since (3.1) represents detailed multibodied properties, it might be suspected that it is demanding too much many-body information from the TDHF wave function. Roughly the same information, however, may be obtained by evaluating the number (or charge) dispersion, $\langle \hat{N}_R^2 \rangle - \langle \hat{N}_R \rangle^2$ as described in Ref. 10. Thus, Table I really deals with the expectation value of only a two-body operator. It remains an open question as to how meaningful expectation values of many-body operators are in the TDHF theory.

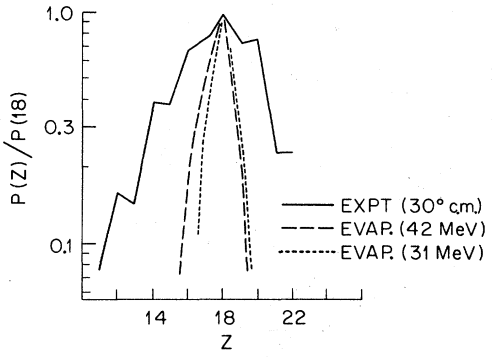

FIG. 8. Fragment charge distribution relative to $Z = 18$ for final states measured in Ref. 21 and calculated due to evaporation.

D. Ion-ion potential

Using the results of our calculations, it is possible to define an interaction potential between colliding ions to facilitate comparisons with other theories. In order to do this, we define the ion-ion potential $V(R)$ by the requirement that the motion of the relative separation coordinate R [cf. Eq. (2.13)] as the ions approach one another be given by

$$\mu \frac{d^2R}{dt^2} = -\frac{dV(R)}{dR}, \tag{3.2}$$

where μ is the reduced mass. Equation (3.2) may be integrated to give

$$V(R) = E - \tfrac{1}{2}\mu \left(\frac{dR}{dt}\right)^2, \tag{3.3}$$

with the integration constant, E, the center-of-mass bombarding energy. By taking dR/dt from our calculations, $V(R)$ may be computed. Note that

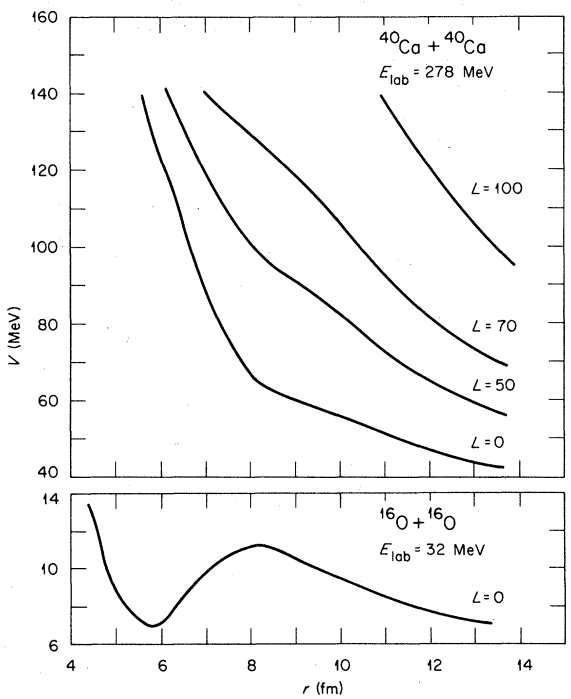

FIG. 9. The TDHF ion-ion potential $V(R)$ for various ^{40}Ca + ^{40}Ca and ^{16}O + ^{16}O systems.

although (3.2) does not allow for dissipation or a coordinate-dependent mass, it may easily be generalized to allow the determination of these quantities from TDHF calculations.[23]

In Fig. 9, we plot $V(R)$ for several $^{40}Ca+^{40}Ca$ systems at a laboratory bombarding energy of 278 MeV and for a head-on $^{16}O+^{16}O$ collision at a laboratory energy of 32 MeV. Of course, these potentials include Coulomb and centrifugal forces. We note that the $^{16}O+^{16}O$ barrier height of 11 MeV is in excellent agreement with the experimentally determined barrier.[24]

The elastic scattering of heavy ions empirically determines the real part of the nuclear potential at the strong absorption radius $R=1.5$ fm $(A_1^{1/3}+A_2^{1/3})$ to be approximately -1 MeV for all systems.[25] Subtracting the point Coulomb energy from the ^{16}O potential in Fig. 9, the nuclear potential at $R=7.6$ fm is found to be -1.1 MeV. A similar calculation for the $l=0$ curve of $^{40}Ca+^{40}Ca$ gives -1.0 MeV at $R=10.3$ fm, in good agreement with the empirical result.

The curves in Fig. 9 and their interpretation deserve some comment. Recall that the crucial assumption is that Eq. (3.2) provides an adequate description of the dynamics. This may not be true for several reasons. First, as has already been mentioned, we have omitted dissipation and a variable mass, features which will undoubtedly modify $V(R)$, especially for small R. Second, since heavy-ion reaction dynamics may require the explicit dynamical treatment of several macroscopic variables, the dynamical form of (3.2) may be inadequate. Indeed, while Fig. 7 has been calculated using the approaching portion of the reaction, the use of the receding portion would yield a different $V(R)$. Third, all of the collective kinetic energy may not be accounted for in (3.3). Finally, the definition of R itself is not unique, and would be expected to be most deficient for fused shapes. Since the above considerations apply most strongly to deeply penetrating trajectories, we believe $V(R)$ most accurate for R greater than or equal to the barrier radius. In future studies, investigation of the energy and angular momentum dependence of V, which automatically includes ion polarization and nonadiabatic effects, will be of great interest.

IV. SUMMARY

We have presented TDHF calculations which use an effective interaction resulting in a local HF potential. Our calculations were constrained to axial symmetry, and relative orbital motion treated in a rotating-frame approximation.

We discussed the details of the time-dependent densities and showed how they were related to the dynamics of the single-particle wave functions and the effects of the Pauli principle. We computed finite impact parameter collisions for $^{16}O+^{16}O$ and $^{40}Ca+^{40}Ca$ and obtained deflection functions and energy loss as a function of impact parameter. While the deflection functions appear consistent with experiment, we obtain too little dissipation. It is an open and essential question as to whether this lack of dissipation arises from the rotating frame approximation, axial symmetry, the freezing of spin-isospin degrees of freedom, the form of the effective interaction used, or is, in fact, intrinsic to the TDHF approximation itself. In this connection, it should be noted that three-dimensional calculations for $^{16}O+^{16}O$ result in fusion for angular momenta for which no fusion occurred in the axially symmetric calculations,[17] although the near head-on collisions and orbiting behavior appear to be at least qualitatively described by the latter calculations. Further calculations are in progress to determine the role of axial symmetry, spin-isospin modes, and the effective interaction.

We presented a brief discussion as to how fragment charge and mass distributions may be extracted from the TDHF wave function. The calculated charge distribution for $^{40}Ca+^{40}Ca$ at $E_{lab}=278$ MeV appears to be narrower than experimental results. We also discussed the determination of an ion-ion potential from TDHF calculations and found the potentials for $^{16}O+^{16}O$ and $^{40}Ca+^{40}Ca$ to be in agreement with phenomenological results. In addition, the calculated $^{16}O+^{16}O$ interaction barrier was found to be in agreement with experiment.

Besides demonstrating that large-scale TDHF calculations are feasible, we have shown how the TDHF dynamics originally investigated for colliding slabs generalize in a more realistic geometry and reproduce many of the essential features of heavy-ion reactions. With our present technology, it is possible to perform realistic axially symmetric calculations for such systems as $^{84}Kr+^{209}Bi$ using a nonlocal Skyrme interaction and allowing for isospin degrees of freedom. Since systems larger than $^{40}Ca+^{40}Ca$ do not presently appear to be tractable in a fully three-dimensional calculation, continued exploration of axially symmetric calculations seems vital.

ACKNOWLEDGMENTS

The authors are grateful to J. Ginocchio for assistance in the calculation of evaporation from the excited reaction products. We would also like to thank M. Baranger and J. R. Nix for several helpful discussions. Three of us (SEK, SJK, and JWN)

would like to thank the Oak Ridge Associated Universities for supporting visits to the Oak Ridge National Laboratory.

APPENDIX A: NUMERICAL METHODS FOR THE TDHF EQUATIONS

In this appendix, we outline the numerical procedures employed for solving the TDHF equations. For simplicity, we treat the motion of a single-particle in a time-dependent potential W. We take W to be axially symmetric and work in cylindrical coordinates (r, z, ϕ). The expressions we derive are directly applicable to the TDHF equations, provided W is taken to be the self-consistent HF potential.

In order to derive unitary evolution expressions and preserve the stationary nature of the TDHF action, we derive the finite difference equations by the discrete analog of the variational form of the Schrödinger equation:

$$\frac{\delta}{\delta\Psi^*(\vec{r})}\left[\langle\Psi^*|i\hbar(\partial/\partial t)|\Psi\rangle-\langle\Psi^*|\hat{H}|\Psi\rangle\right]=0, \tag{A1}$$

where the Hamiltonian functional is

$$\langle\Psi^*|\hat{H}|\Psi\rangle=\int d^3r\,\Psi^*(\vec{r})\left[-\frac{\hbar^2}{2m}\nabla^2+W(\vec{r},t)\right]\Psi(\vec{r}). \tag{A2}$$

Letting $\Psi(\vec{r},t)=(e^{i\mu\phi}/\sqrt{2\pi})\psi(r,z,t)$, where μ is the conserved azimuthal quantum number, (A1) becomes

$$\frac{\delta}{\delta\psi^*(r,z)}\left\{\int rdrdz\left[\psi^* i\hbar\frac{\partial\psi}{\partial t}-\frac{\hbar^2}{2m}\left|\frac{\partial\psi}{\partial r}\right|^2-\frac{\hbar^2}{2m}\left|\frac{\partial\psi}{\partial z}\right|^2-\psi^*\left(W+\frac{\hbar^2\mu^2}{2mr^2}\right)\psi\right]\right\}=0. \tag{A3}$$

Of the various possible discretizations of (A3), which differ with respect to mesh choices and integrations by parts, it is particularly convenient to use the mesh

$$r_j=(j-\tfrac{1}{2})\Delta r,\quad j=1,2,\ldots,N_R \qquad z_k=(k-1)\Delta z,\quad k=-N_Z,-N_Z+1,\ldots,N_Z, \tag{A4}$$

and to discretize (A3) as[19]

$$\frac{\delta}{\delta\psi^*_{jk}}\left\{\sum_{j=1}^{N_R-1}\sum_{k=-N_Z}^{N_Z-1} r_j\,\Delta r\Delta z\left[\psi^*_{jk}\,i\hbar\frac{\partial\psi_{jk}}{\partial t}-\frac{\hbar^2}{2m}\left|\frac{\psi_{j+1k}-\psi_{jk}}{\Delta r}\right|^2\frac{r_{j+1/2}}{r_j}-\frac{\hbar^2}{2m}\left|\frac{\psi_{jk+1}-\psi_{jk}}{\Delta z}\right|^2-\psi^*_{jk}\left(W_{jk}+\frac{\hbar^2\mu^2}{2mr_j^2}\right)\psi_{jk}\right]\right\}=0, \tag{A5}$$

where $\psi_{jk}=\psi(r_j,z_k)$, $W_{jk}=W(r_j,z_k)$. In writing this expression, we have assumed the boundary conditions $\psi_{N_Rj}=0$, $\psi_{iN_Z}=\psi_{i-N_Z}=0$, and have included the factor $r_{j+1/2}/r_j$ in the radial derivative term to account for the fact that $|\partial\psi/\partial r|^2$ is approximated midway between the radial mesh points. Performing the variation in (A5) and introducing $g_{jk}=\sqrt{r_j}\,\psi_{jk}$,[26] we obtain

$$i\hbar\frac{\partial}{\partial t}g_{jk}=(Hg)_{jk}+(Vg)_{jk}, \tag{A6}$$

where the Hermitian horizontal and vertical Hamiltonian operators H and V are defined by

$$(Hg)_{jk}=-\frac{\hbar^2}{2m(\Delta z)^2}\left(g_{jk+1}+g_{jk-1}-2g_{jk}\right)+\tfrac{1}{2}W_{jk}g_{jk}, \tag{A7a}$$

$$(Vg)_{jk}=-\frac{\hbar^2}{2m(\Delta r)^2}\left(C_j g_{j+1k}+C_{j-1}g_{j-1k}-2g_{jk}\right)+\left(\tfrac{1}{2}W_{jk}+\frac{\hbar^2\mu^2}{2mr_j^2}\right)g_{jk}. \tag{A7b}$$

The coefficients C_j are

$$C_j=\frac{j}{(j^2-\frac{1}{4})^{1/2}}\ . \tag{A8}$$

Equations (A6) and (A7) represent a spatial discretization of the single-particle Schrödinger equation. To perform the time discretization, we temporarily suppose W time-independent, and define a time mesh

$$t_n=n\Delta t,\quad n=0,1,2,\ldots.$$

Given the wave function at time t_n, $g^{(n)}_{jk}$, we evolve to t_{n+1} by the Peaceman-Rachford method[27]:

$$g^{(n+1)}=\left[\frac{1}{1+(i\Delta t/2\hbar)V}\right]\left[\frac{1-i(\Delta t/2\hbar)H}{1+i(\Delta t/2\hbar)H}\right]\times\left(1-i\frac{\Delta t}{2\hbar}V\right)g^{(n)}, \tag{A9}$$

where 1 is the unit operator. As can readily be seen by expansion, this expression approximates the exact time evolution operator $\exp[-i(H+V)\Delta t/\hbar]$ through terms in $(\Delta t)^2$, even if H and V do not commute. Furthermore, as can be seen by

applying (A9) for several time steps, it results in almost unitary evolution. The advantage of (A9) is that it involves only operations with sparse matrices. The exact evolution operator is a dense matrix containing some 10^6 nontrivial complex elements for typical mesh sizes, and is so far too large to handle simply. However, the matrices representing H and V are tridiagonal, so that the inversions requires by (A9) may be performed very rapidly by Gaussian elimination.[28] It should be added that since we need only consider the $z \geq 0$ half of the system for symmetric collisions, the operations in (A9) are truncated at $z = 0$ utilizing the (conserved) z parity of the wave function.

An alternative to the Peaceman-Rachford method would be evolution by the operator

$$\left[1-\frac{i\Delta t}{2\hbar}(H+V)\right]\Big/\left[1+\frac{i\Delta t}{2\hbar}(H+V)\right],$$

which requires inversion of a symmetric band matrix of half band width N_R+1 instead of width 2 in the Peaceman-Rachford method. Although this alternative would be exactly unitary, it is only accurate to order $(\Delta t)^2$ and the additional band width does not appear warranted.

In the TDHF problem, the operators H and V are time dependent due to W. In that case, they should be evaluated at $t_{n+1/2}$ in Eq. (A9). To accomplish this, we have used the double stepping method described in the Appendix B of Ref. 10. However, instead of averaging h to get $h^{n+1/2}$, we have averaged ρ to get $\rho^{n+1/2}$ and then constructed $h^{n+1/2}$ from this. This distinction is important only for the three-body term. Other methods of extrapolating the density to $\rho^{n+1/2}$ were investigated, such as utilizing the equation of continuity or polynomial extrapolation from previous time steps, but these were not as stable as the double stepping.

Typical mesh spacings were $\Delta r = \Delta z = 0.4$ fm, with $N_R = 20$ and $N_Z = 60$ or 80 for ^{16}O and ^{40}Ca, respectively (30 or 40 points for $z \geq 0$). The time step Δt was 2.5×10^{-24} s. The results of our calculations are insensitive to these parameters. The total energy of the system is conserved to within ~1.5 MeV out of several hundred during the course of the collision (and better if Δt is made even smaller). The normalization of the single-particle wave functions is constant to within one part in 10^4.

APPENDIX B: EVALUATION OF THE YUKAWA AND COULOMB POTENTIALS

In order to determine the Yukawa potential [cf. Eq. (2.8)]

$$\Phi(\vec{r}) = V_0 \int d^3r'\, \rho(\vec{r}\,') \frac{e^{-|\vec{r}-\vec{r}\,'|/a}}{|\vec{r}-\vec{r}\,'|/a} \tag{B1}$$

and the Coulomb potential

$$\Phi_C(\vec{r}) = \frac{e^2}{4} \int d^3r'\, \rho(\vec{r}\,') \frac{1}{|\vec{r}-\vec{r}\,'|}\,, \tag{B2}$$

we must solve, respectively, the Helmholtz equation

$$-\nabla^2\Phi(\vec{r}) + (1/a^2)\Phi(\vec{r}) = 4\pi\, a\, V_0\, \rho(\vec{r}), \tag{B3}$$

and the Poisson equation

$$-\nabla^2\Phi_C(\vec{r}) = 4\pi\tfrac{1}{4}e^2\rho(\vec{r}). \tag{B4}$$

The latter equation is, of course, a special case of the former. In particular, we may obtain Eq. (B4) by taking the limit of Eq. (B3) in which

$$a \to \infty, \quad V_0 \to 0, \quad V_0 a \to \tfrac{1}{4}e^2\,.$$

It therefore suffices to discuss the numerical solution of Eq. (B3). We will, however, have to treat the boundary conditions at infinity in a different manner in the two cases.

Since the solution of (B3) is axially symmetric about the axis $r = 0$, we work on the mesh defined by (A4), with

$$\begin{aligned} \phi_{jk} &= \sqrt{r_j}\ \Phi(r_j, z_k), \\ S_{jk} &= \sqrt{r_j}\ 4\pi a V_0 \rho(r_j, z_k). \end{aligned} \tag{B5}$$

Equation (B3) may then be approximated on the mesh by

$$[(H+V)\phi]_{jk} = S_{jk}\,, \tag{B6}$$

where the Hermitian horizontal and vertical Helmholtz operators are defined by

$$(H\phi)_{jk} = -\frac{1}{(\Delta z)^2}(\phi_{jk+1} + \phi_{jk-1} - 2\phi_{jk}) + \frac{1}{2a^2}\,\phi_{jk}, \tag{B7a}$$

$$(V\phi)_{jk} = -\frac{1}{(\Delta r)^2}(C_j\,\phi_{j+1k} + C_{j-1}\phi_{j-1k} - 2\phi_{jk}) + \frac{1}{2a^2}\,\phi_{jk}\,, \tag{B7b}$$

and the coefficients C_j are defined by (A8). The solution to (B6) is given iteratively by[29]

$$\phi^{m+1/2} = \frac{1}{H+R_{m+1}}[(R_{m+1}-V)\phi^m + S]\,, \tag{B8a}$$

$$\phi^{m+1} = \frac{1}{V+R_{m+1}}[(R_{m+1}-H)\phi^{m+1/2} + S]\,. \tag{B8b}$$

The R_{m+1} are acceleration parameters, whose selection is discussed below. As in the case of the Schrödinger equation, the operators H and V are tridiagonal, so that the inversions may be per-

formed by Gaussian elimination. Again for symmetric systems, the symmetry of ϕ restricts the actual numerical work to $z \geq 0$.

The boundary condition for the Yukawa potential may be taken to be $\phi = 0$ on the outer edges of the mesh because of the short range of the Yukawa force. However, the long range of the Coulomb potential forces an explicit evaluation of Eq. (B2) for $\vec{r}$ on the outer mesh edges. Performing the azimuthal integrations, (B2) becomes[30]

$$\phi_C(r, z) = e^2 \int_0^\infty r' dr' \int_{-\infty}^\infty dz' \, \frac{\rho(r', z')\kappa(k)}{[(z-z')^2 + (r+r')^2]^{1/2}} , \tag{B9}$$

where κ is the complete elliptic integral

$$\kappa(k) = \int_0^{\pi/2} \frac{dx}{(1-k^2 \sin^2 x)^{1/2}} \tag{B10}$$

and $k = 4rr'/[(z-z')^2 + (r+r')^2]^{1/2}$. We have evaluated (B9) on the mesh edge by Simpson's rule using fourth degree polynomial approximations to (B10).[31] We note that for the Coulomb potential, a direct evaluation of (B2) over the whole mesh would require $\sim N_R \cdot N_Z$ foldings of the form (B9), whereas the determination of ϕ_C on the boundaries requires only $N_R + N_Z$ foldings. The additional numerical work of then solving (B8) is negligible. We have found it necessary to recompute (B9) on the mesh edge only once every four time steps. When this is done, we solve (B8) to $m = 6$ to assure adequate convergence.

Because Eqs. (B8) determine the potential iteratively, a proper guess for the solution will speed the convergence process. At time $t = 0$, any initial guess for the potentials will do (e.g., the zero-range solution $\phi_{jk} = a^2 S_{jk}$ for the Yukawa) and convergence is achieved by iterating (B8) to $m \sim 20$. After the first time step, an excellent guess for the potential at time t_{n+1} is the potential at time t_n. Thus, during the evolution, (B8) need only be iterated to $m = 2$.

The values of the acceleration parameters R_m are taken as in Varga.[32] The eigenvalues of H are bounded from below by

$$\alpha = \frac{\pi^2}{4(N_Z - 1)^2 (\Delta z)^2} + \frac{1}{2a^2} ,$$

while the eigenvalues of V may be approximately bounded from above by

$$\beta = \frac{\pi^2}{(\Delta r)^2} + \frac{1}{2a^2} .$$

The optimal values of R_m for a two-step iteration are then

$$R_m = \begin{cases} \gamma - (\gamma^2 - \alpha\beta)^{1/2}, & m \text{ even}, \\ \gamma + (\gamma^2 + \alpha\beta)^{1/2}, & m \text{ odd}, \end{cases}$$

with $\gamma = (\alpha\beta)^{1/4} [\frac{1}{2}(\alpha+\beta)]^{1/2}$. Although it is possible to use a one-step iteration with $R_m = \sqrt{\alpha\beta}$ for all m, we have found its convergence poorer than the two-step method.

APPENDIX C: EXTRACTION OF MASS TRANSFER IN TDHF

Using the ordinary probability interpretation of the many-body wave function Ψ, Eq. (3.1) straightforwardly gives the probability of finding any A_L nucleons in the lefthand fragment ($z < 0$) and any $A_R = A - A_L$ nucleons in the righthand fragment ($z \geq 0$), assuming $|\Psi|^2$ to be a symmetric function of all its arguments. Using the fact that the TDHF wave function is a Slater determinant, (3.1) may be written in terms of the single-particle wave functions ψ_α, as

$$P(A_R) = \frac{1}{A_L! A_R!} \sum_{PP'} (-)^{P+P'} N^R_{P1P'1} \cdots N^R_{PA_RP'A_R} \times N^L_{P(A_R+1)P'(A_R+1)} \cdots N^L_{PAP'A} , \tag{C1}$$

where the left and right overlaps are defined as (all other integration variables suppressed):

$$N^R_{\alpha\beta} = \int_0^\infty dz \, \psi^*_\alpha(z)\psi_\beta(z), \quad N^L_{\alpha\beta} = \int_{-\infty}^0 dz \, \psi^*_\alpha(z)\psi_\beta(z),$$

$$N^R_{\alpha\beta} + N^L_{\alpha\beta} = \delta_{\alpha\beta}. \tag{C2}$$

P and P' are permutations of the A indices and Pi denotes the action of P on the index i. For fixed P, the sum over P' results in the term

$$(-)^P \det \begin{bmatrix} N^R_{P11} & N^R_{P12} & \cdots & N^R_{P1A} \\ \vdots & \vdots & & \vdots \\ N^L_{P(A_R+1)1} & N^L_{P(A_R+1)2} & \cdots & N^L_{P(A_R+1)A} \\ \vdots & \vdots & & \vdots \end{bmatrix} .$$

The various P permutations may be viewed as interchanging the $A_R R$ and the $A_L L$ labels with the appropriate sign. However, for any combination of A_R rows labeled R and A_L rows labeled L, there are $A_L! A_R!$ different P which result in no change in the value of the determinant. Thus (C1) takes the form

$$P(A_R) = \sum_{\substack{\text{combinations} \\ \text{of } A_R R \text{ rows} \\ \text{and } A_L L \text{ rows}}} \det \begin{bmatrix} N^R_{11} & N^R_{12} & \cdots \\ \vdots & & \\ N^L_{1j} & \cdots & \ddots \end{bmatrix} .$$

Note that $\sum_{A_R=0}^{A} P(A_R) = \det[N^R_{\alpha\beta} + N^L_{\alpha\beta}] = 1$, as expected.

Because our wave functions possess good angular momentum projection along the z axis, μ, each determinant in (C2) factorizes into a product of determinants for each value of μ. This property facilitates the numerical evaluation of $P(A_R)$:

$$P(A_R) = \sum_{\{n_\mu\}} \delta\left(\sum_{\mu=-\mu_{\max}}^{\mu_{\max}} n_\mu,\ A_R \right) \prod_{\mu=-\mu_{\max}}^{\mu_{\max}} P_\mu(n_\mu), \tag{C3}$$

where $P_\mu(n_\mu)$ is the determinant giving the probability of finding n_μ nucleons with orbital angular momentum projection μ in the right-hand fragment and $\mu_{\max}$ is the maximum azimuthal quantum number in the system.

For the special case of spin-saturated, charge symmetric systems, P_μ is block diagonal, the blocks corresponding to the various spin-isospin states of a nucleon. Furthermore, for a given number of right-hand nucleons, the value of each block is independent of spin-isospin state. In addition, $P_\mu = P_{-\mu}$, and for reflection symmetric systems, $P_\mu(n_\mu)$ is symmetric about half the maximum value of its argument.

---

*This work was sponsored in part by the U.S. Energy Research and Development Administration under contract with Union Carbide Corportation.

†Supported in part by the National Science Foundation [MPS71-02670 A05].

‡On leave from Institut für Kernphysik, Technische Hochschule Darmstadt, Darmstadt, West Germany.

§Permanent address: Department of Physics, University of Illinois at Chicago Circle, Chicago, Illinois 60680.

¶Alfred P. Sloan Foundation Research Fellow.

[1]J. A. Wheeler, Phys. Rev. 52, 1083, 1107 (1937).

[2]D. L. Hill and J. A. Wheeler, Phys. Rev. 89, 1102 (1953).

[3]A. de-Shalit and H. Feshbach, *Theoretical Nuclear Physics*, (Wiley, New York, 1974) Vol. 1, p. 541.

[4]S. T. Belyaev, Nucl. Phys. 64, 17 (1965); F. M. H. Villars, in *Dynamic Structure of Nuclear States, Proceedings of the 1971 Mont Tremblant International Summer School*, edited by D. J. Rowe (Univ. of Toronto Press, Toronto, 1972); M. Baranger, J. Phys. 33, C5-61 (1972).

[5]K. T. R. Davies, A. J. Sierk, and J. R. Nix, Phys. Rev. C 6, 2385 (1976); J. R. Nix and A. J. Sierk, Report No. LA-UR-75-1643 (unpublished) [presented at the International School-Seminar on Reactions of Heavy Ions with Nuclei and Synthesis of New Elements, Dubna, USSR, Sept. 23–Oct. 4, 1975 (unpublished)]; A. J. Sierk and J. R. Nix, Lemon Aid Report No.-151 [presented at the Symposium on Macroscopic Features of Heavy-Ion Collisions, Argonne National Laboratory, Argonne, Illinois, April 1–3, 1976 (unpublished)].

[6]D. M. Brink, K. Goeke, S. J. Krieger, and D. Vautherin, Nucl. Phys. A249, 215 (1975).

[7]S. J. Krieger and K. Goeke, Nucl. Phys. A234, 269 (1974).

[8]S. E. Koonin, Ph.D. thesis, Massachusetts Institute of Technology, 1975 (unpublished); C. Y. Wong, J. A. Maruhn, and T. A. Welton, Nucl. Phys. A256, 469 (1975).

[9]P. A. M. Dirac, Proc. Camb. Phil. Soc. 26, 376 (1930).

[10]P. Bonche, S. E. Koonin, and J. W. Negele, Phys. Rev. C 13, 1226 (1976).

[11]T. H. R. Skyrme, Phil. Mag. 1, 1043 (1956); M. Beiner, H. Flocard, Nguyen Van Giai, and P. Quentin, Nucl. Phys. A238, 29 (1975).

[12]G. F. Bertsch and S. F. Tsai, Phys. Lett. 50B, 319 (1974); G. F. Bertsch and S. F. Tsai, Phys. Rep. 18C, No. 2, May (1975).

[13]S. E. Koonin, Phys. Lett. 61B, 227 (1976).

[14]R. Y. Cusson and J. Maruhn, Phys. Lett. 62B, 134 (1976); R. Y. Cusson, R. K. Smith, and J. A. Maruhn, *ibid.* 36, 1166 (1976).

[15]A preliminary account of this work has been given by S. E. Koonin, in Proceedings of the International Workshop IV on Gross Properties of Nuclei and Nuclear Excitations, edited by W. D. Myers (unpublished).

[16]A. Kerman and S. E. Koonin, Ann. Phys. 100, 332 (1976).

[17]S. E. Koonin and M. Stillerman (unpublished).

[18]H. Feldmeier (unpublished).

[19]J. W. Negele, in Proceedings of the International Workshop IV on Gross Properties of Nuclei and Nuclear Excitations, edited by W. D. Myers (unpublished).

[20]P. Möller and J. R. Nix, Nucl. Phys. A272, 502 (1976).

[21]P. Colombani, N. Frascuria, J. L. Jacmart, M. Riou, C. Stéphan, H. Doubre, N. Poffé, and J. C. Roynette, Phys. Lett. 55B, 45 (1975).

[22]I. Dostrovsky and Z. Fraenkel, Phys. Rev. 116, 683 (1959).

[23]S. E. Koonin and A. Axelrod (unpublished).

[24]D. A. Bromley, J. A. Kuehner, and E. Almqvist, Phys. Rev. 123, 878 (1961).

[25]G. R. Satchler (private communication).

[26]Y. Boneh and Z. Fraenkel, Phys. Rev. C 10, 893 (1974); Y. Boneh, Lawrence Berkeley Laboratory Report, 1975 (unpublished).

[27]R. Varga, *Matrix Iterative Analysis* (Prentice-Hall, Englewood Cliffs, 1962), p. 273.

[28]R. Varga, *Matrix Iterative Analysis* (see Ref. 27), p. 195.

[29]R. Varga, *Matrix Iterative Analysis* (see Ref. 27), p. 209.

[30]K. T. R. Davies and A. J. Sierk, J. Comp. Phys. 18, 311 (1975).

[31]M. Abramowitz and I. Stegun, *Handbook of Mathematical Functions* (Dover, New York, 1965), p. 591.

[32]R. Varga, *Matrix Iterative Analysis* (see Ref. 27), p. 230.

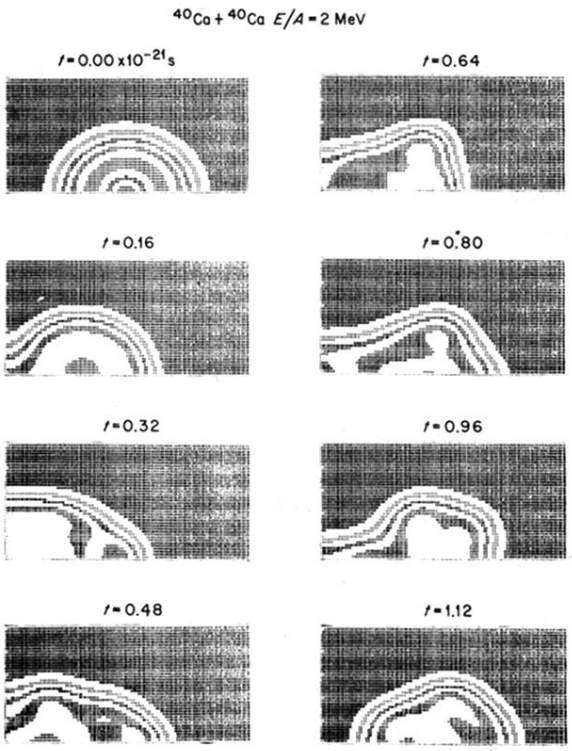

FIG. 2. Similar to Fig. 1 for a head-on $^{40}Ca + ^{40}Ca$ collision at a laboratory bombarding energy of 8 MeV/nucleon. This figure and all those subsequent have been calculated using (2.8).